Imaging Global Seismic Phase Arrivals by Stacking Array Processed Short-Period Data

Sebastian Rost,[1,2] Michael S. Thorne,[2,3] and Edward J. Garnero[2]

INTRODUCTION

For decades, seismic data stacking has been used to improve the signal-to-noise ratio (SNR) of coherent arrivals in seismic recordings. Seismic arrays are especially well-suited for this task and have been used to detect and identify typically weak seismic arrivals (*e.g.,* Birtill and Whiteway 1965; Green *et al.* 1965). Seismic arrays are deployments of no fewer than three seismometers with uniform instrumentation that allow the recorded time series to be stacked as an ensemble. Typical array apertures range from 2 km to 200 km (Rost and Garnero 2004) and consist of 10 to 100 stations. All seismic array elements receive a centralized time signal, minimizing possible timing errors. Stations are deployed in specialized configurations to ensure a high coherence of transient signals in the wavefield, while the statistical noise component is uncorrelated between stations (Haubrich 1968).

Special techniques have been developed to process seismic array data (for a review, see Rost and Thomas 2002), enabling the use of subtle arrivals in the seismic wavefield for seismic analysis and thus holding promise for higher resolution snapshots of the structure of the Earth's interior (*e.g.*, Vidale and Benz 1993; Vidale and Earle 2000; Rost *et al.* 2005b). With increasing numbers of temporary and permanent array installations, data are becoming readily available for further high-resolution studies of the Earth's interior.

In this paper we present a method to extract array-specific information (*e.g.,* vertical incidence angle-slowness) from a large number of array recordings. Slowness, time, and amplitude information from array recordings of individual earthquakes are combined into a single summary trace per earthquake, then stacked with other summary traces from a multitude of earthquakes recorded at the same seismic array. As a test case we process short-period array data from the Canadian Yellowknife Array (YKA) to highlight seismic phases that sample the whole of the Earth's interior. The stacked array data emphasize the detectability of seismic phases in the short-period seismic wavefield. This effort is similar to those of Astiz *et al.* (1996) and Earle (1999), with the notable exception that our array analyses allow us to retain wave slowness information.

The first section of this paper introduces the seismic data selected for this study and discusses the techniques used to preprocess these data. The second section gives an overview of the main processing steps used to produce new travel-time maps of the short-period seismic wavefield. Lastly, the third section shows results of applying these processing techniques: We present several seismic arrival maps of data collected from shallow earthquakes. We discuss interesting observations in these arrival maps and highlight the utility of global array data stacks. Because the software tools used in this study could be useful for a wide range of applications from the classroom to research, we provide a brief description of the algorithms and software used here. All data and scripts used to produce figures in this manuscript are provided on the World Wide Web at http://array-seismology.asu.edu.

ARRAY DATA AND PREPROCESSING

We use data from YKA, a small-aperture array consisting of 19 short-period, vertical component instruments with a dominant response frequency of approximately 1 Hz. The array aperture is 20 km with instruments deployed along two perpendicular lines (in N-S and E-W directions) with an interstation spacing of 2.5 km. YKA was designed specifically to detect high-frequency *P* waves and is therefore especially well-suited to study the short-period seismic wavefield at regional and teleseismic distances (Weichert and Whitham 1969).

For this study, we use earthquakes recorded from January 2000 to December 2004, collected from EarthquakesCanada of the Geological Survey of Canada (http://www.earthquakescanada.nrcan.gc.ca). We selected all available shallow events (depths less than 40 km) with magnitudes (m_b) larger than 5.5, resulting in an initial dataset of 1,836 earthquakes. Seismograms with obvious data errors, such as gaps and spikes, were discarded. We also omitted events that were recorded by fewer than 10 stations. After applying a fourth-order Butterworth band-pass filter with cutoff frequencies of 0.5 Hz and 1.4 Hz, we further removed events from the dataset that did not display visually coherent energy in the seismograms. Following these steps, recordings with extremely long *P* coda (more than 250 s) or small SNR of the initial arrival were additionally removed. This resulted in a final dataset consisting of 1,224 earthquakes.

1. School of Earth and Environment, Earth Sciences, University of Leeds.
2. Department of Geological Sciences, Arizona State University.
3. Arctic Region Supercomputing Center, University of Alaska Fairbanks.

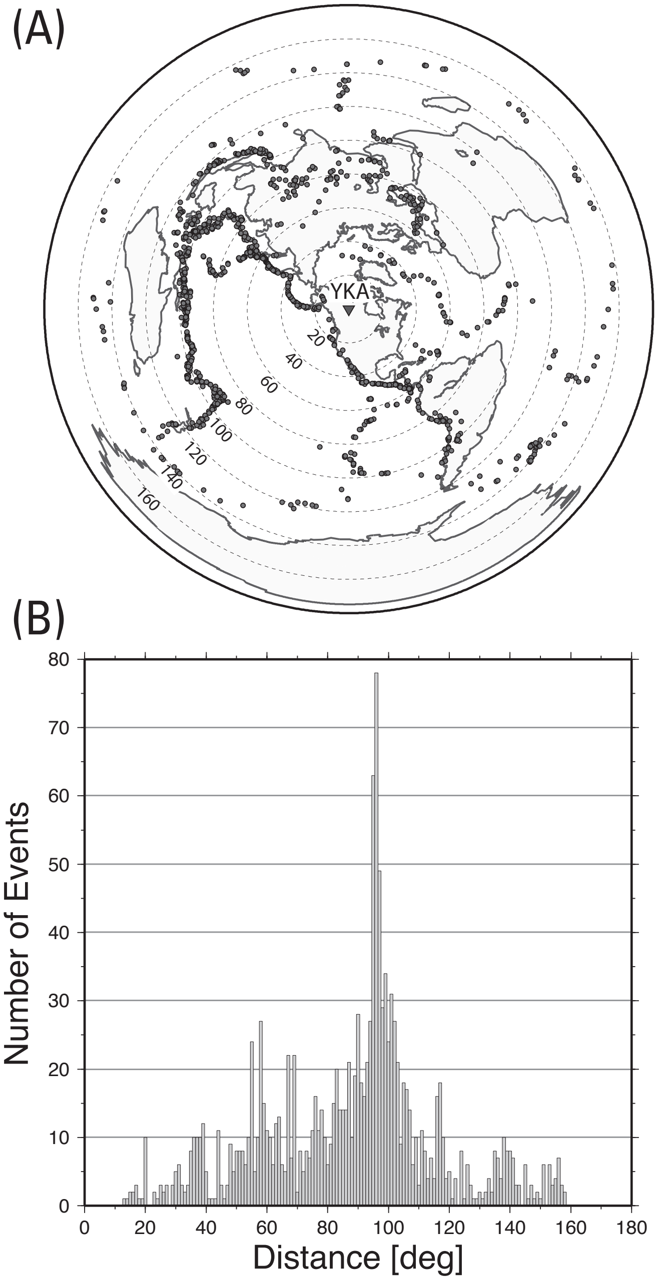

▲ **Figure 1.** (A) Map centered on the YKA location (triangle) showing the 1,224 shallow events of the final dataset (dark circles) with $m_b \geq 5.5$. Earthquakes are shown with respect to epicentral distance to YKA with dashed circles denoting 20° distance bins. (B) Histogram of number of events in 1° epicentral distance bins for the earthquakes shown in figure 1(A).

The geographical distribution of events is shown in figure 1(A). Due to the location of major earthquake belts relative to YKA, our dataset is distributed unevenly in epicentral distance (figure 1(B), summed in 1° distance bins). The dataset does not contain earthquakes with epicentral distances closer than ~10° or larger than ~160°. We note a large spike in the distribution between 95° to 100° due to the seismically active subduction zones in the southwestern Pacific.

We apply two stacking algorithms to the data: (1) *n*th-root stacking (Kanasewich *et al.* 1973; McFadden *et al.* 1986) and (2) phase-weighted stacking (PWS) (Schimmel and Paulssen 1997). For *n*th-root stacking, the *n*th-root of the individual array station recordings is taken, while preserving the sign of each sample before calculating a vespagram, *i.e.,* a slant stack (Davies *et al.* 1971), whereby summed (beam) traces are calculated for specific incidence angles, *i.e.*, slownesses. This is accomplished by time shifting individual (previously *n*th-rooted) traces according to their location (*i.e.,* distance from a reference station in the array) and the assumed slowness for a fixed back azimuth. After summation, the *n*th power of the beam traces is taken. Again, the sign of each sample is preserved. Normally $n = 4$ is used, but higher (or lower with $n = 1$ being a linear stack) values for n are possible. Here we use $n = 10$ for its higher noise suppression and slowness resolution (Rost and Thomas 2002). *n*th-root processing decreases the amplitude variance of the traces, making the signal coherence more important in the stacks than signal amplitude. Nonetheless, it is not an amplitude-independent stacking scheme.

PWS uses a coherence measure that is unbiased by amplitude. PWS calculates the coherence of the input signals as a function of time to weigh the result of a linear stack (Schimmel and Paulssen 1997). Therefore, signal coherence in the original data is more important for high amplitudes in the resulting stacks than the original signal amplitude. For example, the input signals with the highest amplitudes are only weighted strongly if their signal coherence is also strong. For more information on the array processing schemes used here, see Davies *et al.* (1971), Schimmel and Paulssen (1997), Rost and Thomas (2002), and references therein.

Both stacking techniques are nonlinear and alter the waveforms. Although waveform information is lost by the processing, timing and slowness information are accurately extracted from the stacks. The earthquakes used in this study display a wide variety of source-time functions. As we do not remove or normalize the source-time functions from the individual recordings, we calculate the envelope function of the stacks (Taner *et al.* 1979), thereby avoiding inconsistencies with arrival polarity and phase between earthquakes in additional data processing that follows.

Benefits of array processing of short-period data become obvious in figure 2. Figure 2(A) shows raw recordings of an $m_b = 5.7$ earthquake located at 101.5° epicentral distance from YKA. The individual raw recordings appear noisy, and individual coherent arrivals apart from the first arrival P (P_{diff}) are difficult to detect. Due to the low SNR, arrival times are impossible to measure. Figure 2(B) shows seismic energy $s(u,t)$ as a function of slowness (u) and time (t), from the *n*th-root stacking technique applied to the array data for this earthquake. Stacking was computed for slownesses between –10 s/° and +15 s/°, every 0.3 s/°. Positive and negative slownesses correspond to minor and major arc phases, respectively. Here, we do not consider energy contributions to the stacks arriving off the great circle plane containing the source and receiver. This slowness range includes most major *P*- and *S*-wave phases from regional to teleseismic

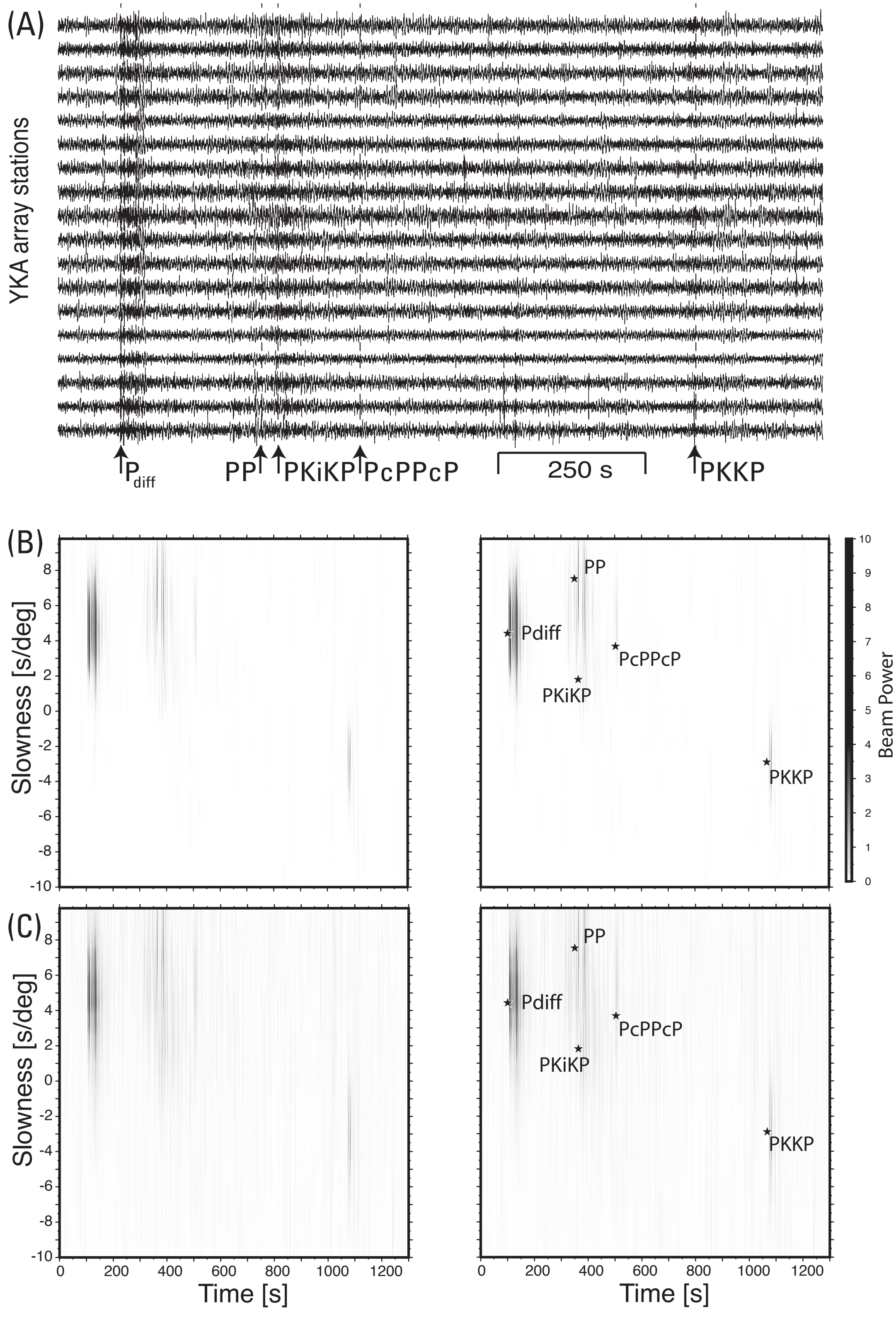

▲ **Figure 2.** (A) Raw seismograms of event on 02 December 2002 UT 13:42 in the northern Molucca region recorded at YKA. Epicentral distance is 101.5° at a depth of 21 km. Event magnitude is $m_b = 5.7$. (B) Tenth-root vespagram of event shown in figure 2(A). The left-hand side shows the unmarked *n*th-root stack while the right-hand display shows the vespagram with marked theoretical travel times (and slownesses) for the 1D Earth model PREM. Marked phases include P_{diff}, *PP*, *PKiKP*, *PcPPcP* and *PKKP*. The phase marked *PcPPcP* shows a slightly larger slowness than predicted by PREM and therefore this energy might be related to *PP* coda. (C) Same as figure 2(B) but for a third-power PWS of event shown in figure 2(A).

distances. The *n*th-root vespagram shows stack amplitude (*i.e.*, beam power) in slowness-time space, and demonstrates how low-amplitude arrivals can be elevated out of the noise, appearing sharp in slowness-time space. In these stacks, a variety of individual arrivals can be identified (a panel to the right indicates phase identification using ray-theoretical travel time and slowness predictions for the Preliminary Reference Earth Model (PREM) radial Earth model (Dziewonski and Anderson 1981). Figure 2(C) shows the phase-weighted stacked data. The PWS is calculated for the same slowness range, but with a third power in the processing. The two methods yield similar results for this example.

STACKING VESPAGRAMS OF GLOBAL EARTHQUAKES

Here we describe construction of a new, high-resolution time series from the nonlinear array stacks described above. For each earthquake, the maximum beam power (A) and its associated slowness u are computed in a sliding time window (*i.e.*, across $s(u,t)$). A new time series is constructed, with amplitudes assigned from A; this summation trace thus contains phase information at slownesses where seismic energy has its maximum amplitude and is referred to as a stack trace $ST_{A,u}(t)$, in other words:

$$ST_{A,u}(t) = \max s(u,t) \qquad \begin{matrix} \{t_1 \le t \le t_2\} \\ \{-10\ \mathrm{s}/^\circ \le u \le +15\ \mathrm{s}/^\circ\}, \end{matrix} \tag{1}$$

with t_1 and t_2 as the upper and lower bounds of the sliding time window, respectively, and slowness u within the bounds of the vespagram (here from –10 s/° to +15 s/°). The resulting stack trace $ST_{A,u}(t)$ thus compacts the time, slowness, and beam power amplitude information contained in the original stack $s(u,t)$ down to a single trace, retaining only time, maximum beam power amplitude, and the slowness at which the maximum beam power occurred. Therefore, $ST_{A,u}(t)$ is a multidimensional time-series that has higher SNR and better temporal resolution of arrivals than any single station recording, and it retains slowness and beam power information. In constructing $ST_{A,u}(t)$ we obtain the best results using a sliding time window with a 1-s width and a 1-s time step increment. The dominant period of the data used is about 1 s and shorter time windows did not lead to clearer arrival detections. The sample increment for $ST_{A,u}(t)$ is therefore 1 s with the slowness and amplitude values centered in the time windows.

Figure 3 demonstrates the construction of $ST_{A,u}(t)$ for the event shown in figure 2. The upper panel identifies maximum amplitudes (scaled by circle diameter) at the slowness of detection for each 1-s time window of the original *n*th-root stack, $s(u,t)$. The resulting stack trace $ST_{A,u}(t)$ is displayed in the lower panel. Shown is the stack amplitude of $ST_{A,u}(t)$ as a function of time. The amplitude of each 1-s time window is shown as one column. The slowness information of $ST_{A,u}(t)$ is shown as grayscaling of the columns with slownesses ranging from –10 s/° to +10 s/°. All the major arrivals in $s(u,t)$ (figure 3, top), P_{diff}, *PP, PKiKP, PcPPcP, PKKP* (which can also be identified in the vespagram), are characterized in $ST_{A,u}(t)$ (figure 3, bottom) by both high stack amplitudes and diagnostic slowness values with evidence for coda phases (*e.g.,* decaying coda amplitudes for P_{diff} between 630 and 700 s) and scattered waves (*e.g.,* increasing amplitudes between 820 and 850 s before the main *PP* arrival).

We apply this procedure to all 1,224 earthquakes in our final dataset for both the *n*th-root stacking and PWS methods. Finally, we construct global stacks of our entire dataset of traces $ST_{A,u}(t)$ in a manner similar to that of Astiz *et al.* (1996). In contrast to Astiz *et al.* (1996), $ST_{A,u}(t)$ contains slowness and amplitude information. In constructing the global stacks we normalize the maximum amplitude of each trace to unity. We then reference all $ST_{A,u}(t)$ traces to earthquake origin time and linearly stack $ST_{A,u}(t)$ amplitudes and slownesses in discrete distance bins. The size of the distance bin is variable in our algorithm with 0.5° distance bins used for the examples given here. The global stacks are combined in record section format in the distance range from 0° to 180° and for the time window from 0 s (origin time) to 2,000 s. To suppress noise further we eliminate any energy with an amplitude ratio smaller than 10 relative to the largest amplitude in each distance bin. Although this processing step might suppress small amplitude arrivals, stronger arrivals are easier to identify. We discuss the results of these stacks in the next section.

RESULTS AND DISCUSSION

We are able to globally stack $ST_{A,u}(t)$ using either slowness, amplitude, or a combination of the two. Pure amplitude stacking of our array data produces results similar to Astiz *et al.* (1996) (figure 4). In calculating the amplitude stack, we detected major phases including the mantle phases *P*, P_{diff}, and *PP*; the core reflected phases *PcP* and *ScP*; the minor arc core phases *PKiKP* and *PKP*; and the major arc core phases *PKKP* and *SKKP*. There is also evidence for slight *S*-wave energy recorded on the vertical-component instruments. Several phases are detected in somewhat abbreviated distance windows, although their travel time curves span larger distance ranges. For example, we only reliably detect *PcP* and *ScP* between ~30° and 60°, although other studies have detected these phases at shorter epicentral distances (*e.g.*, Koper and Pyle 2004). As another example, we only detect *PKiKP* continuously for distance ranges larger than ~100°, although previous studies also have reported observations of *PKiKP* at shorter distances (*e.g.,* Koper and Pyle 2004; Koper and Dombrovskaya 2005). Special source radiation and/or source-receiver combinations may be necessary to detect these phases at distance ranges where we do not observe them. We also note that subtle high-frequency arrivals can be blurred in our global stacking scheme that aligns the stack traces on uncertain published origin times.

Short-term to long-term average ratio functions (STA/LTA) are commonly used with array data for arrival detection (Allen 1982). This algorithm also can be applied to $ST_{A,u}(t)$ (figure 5). The STA/LTA function we use is similar to those used by Shearer (1991) and Astiz *et al.* (1996), although different time-window widths have been used. We compute STA/LTA functions with a STA time window of 10 s and a LTA time window

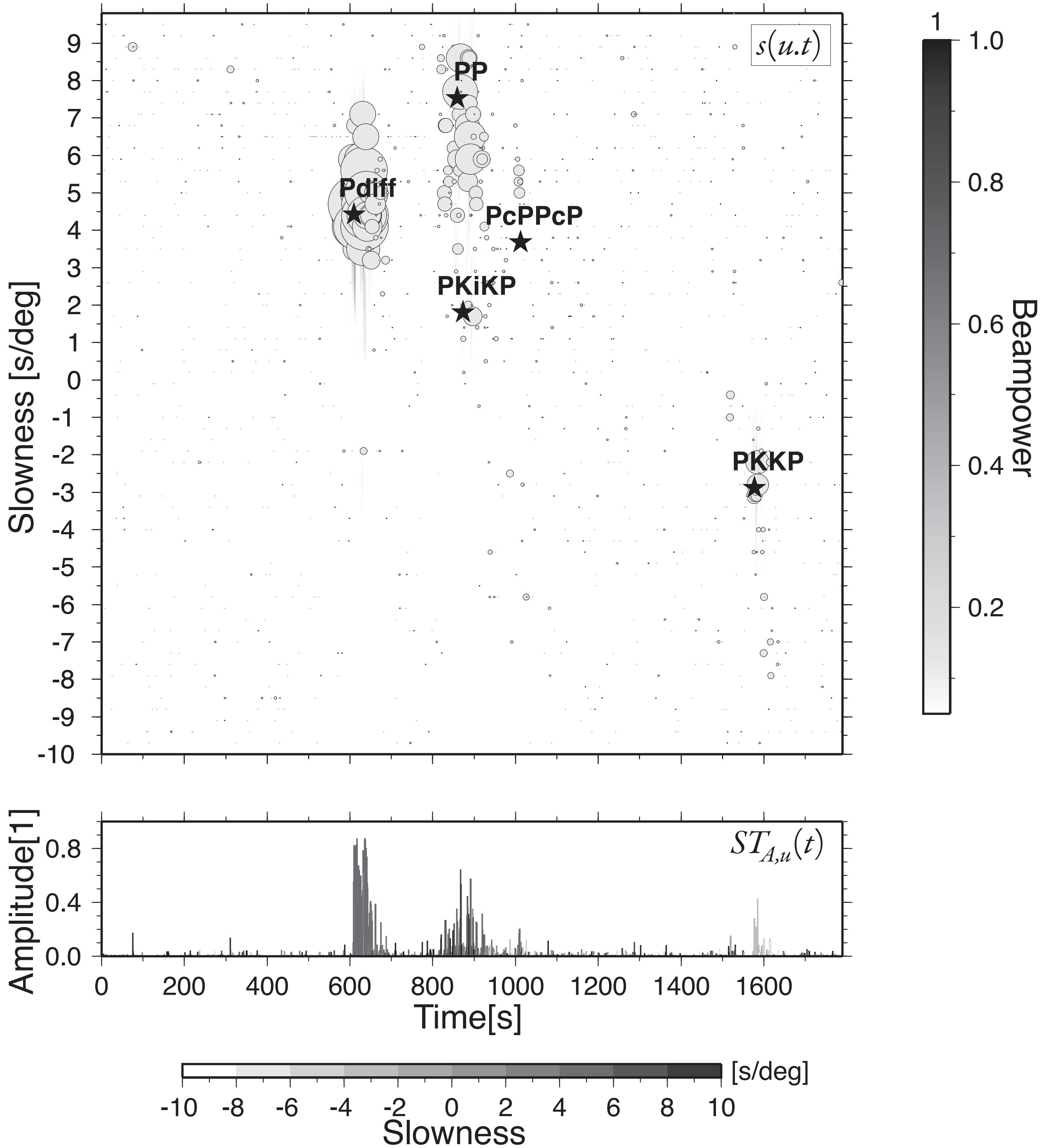

▲ **Figure 3.** Sketch of algorithm used to calculate $ST_{A,u}(t)$. Upper panel shows the *n*th-power stack for the event shown in Figure 2(B). Circles show slowness-time locations of energy maxima in a 1-s moving time window. Slowness is color-coded and the circle diameter shows the beam power for the maximum. Lower panel shows the resulting multidimensional trace retrieved from the nonlinear stack, $ST_{A,u}(t)$. This new time series contains the beam-power amplitude (shown as bar amplitude), timing, and slowness (shown as gray scale) information.

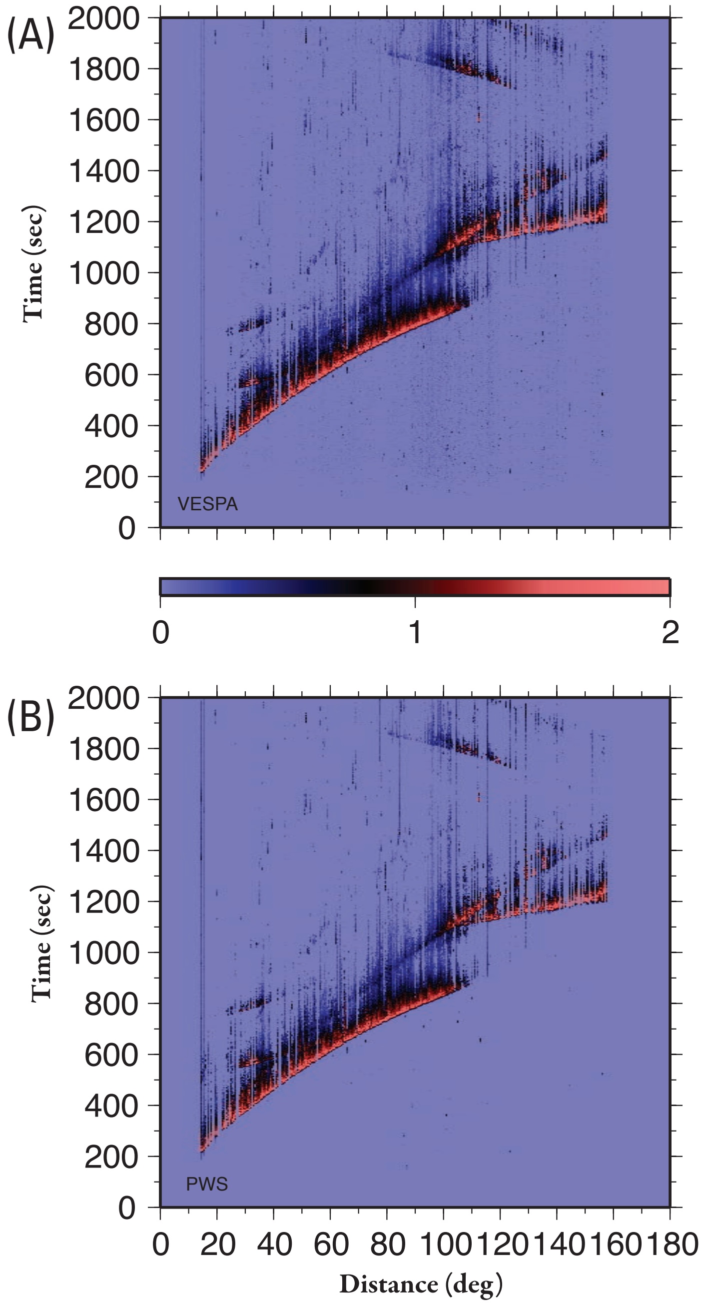

▲ **Figure 4.** (A) Vertical amplitude stacks for the tenth-root processed raw data. A noise gate was applied to suppress noise further. The right-hand side shows the amplitude stacks with overlying travel time curves for PREM. (B) Same as figure 4(A), but for the phase-weighted stack processed raw data.

of 100 s. We use a ratio threshold of 2.5 (figures 5C and 5D) and 3.0 (figure 5A). The STA/LTA function is particularly useful in detecting first arrivals and for suppressing coda energy. Phases detected in the STA/LTA stacks are similar to those in figure 4. Nonetheless, phases with preceding large coda, *e.g.*, *PP* in the presence of *P* (or P_{diff}) coda, are less clear. It is also more difficult to detect triplication phases with the STA/LTA processing.

The addition of slowness information permits more informative global stacking: Figure 6 uses the $ST_{A,u}(t)$ slowness information for color-coding the stacked energy. The base color corresponds to slowness, and color intensity is scaled by beam power. For example, arrivals with slownesses in the range of 5.2 s/° to 6.6 s/° are color-coded green (*e.g.,* the *P*-wave arrival in the distance range from ~60° to 80°) with the highest beam power arriving energy more brightly lit. Conversely, lower beam-power energy is shown with diminishing brightness; energy below the noise threshold cutoff is displayed as black.

Using the slowness information makes phase identification easier, especially in phases that are potentially masked by coda energy. For example, *PP* can be clearly identified in the *P* (and

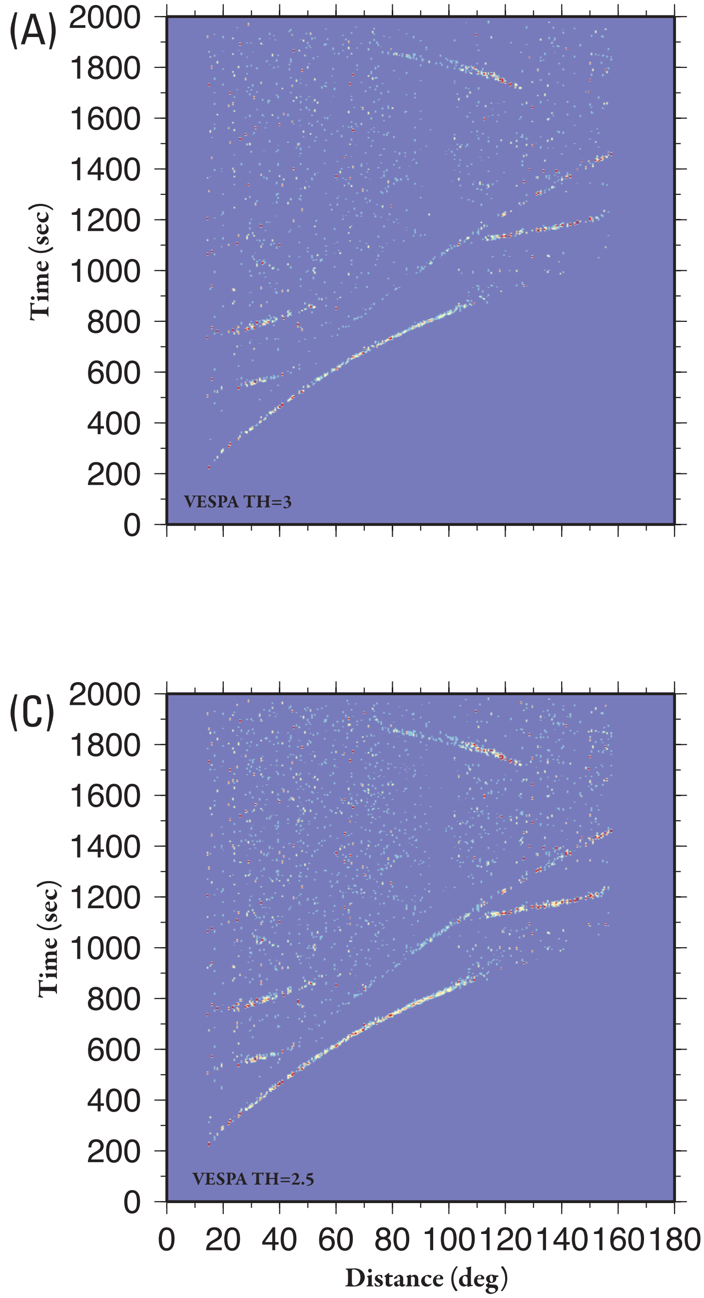

▲ **Figure 5.** STA/LTA ratio processed data. (A) STA/LTA with threshold 3.0 for the vespagram processed data. (B) Travel time curves calculated for PREM. (C) STA/LTA with threshold 2.5 for vespagram processed data. (D) STA/LTA with threshold 2.5 for PWS processed data.

P_{diff}) coda due to its unique (higher) slowness, *i.e.,* shallower incidence angle. Several distance-time windows (figure 6B) show interesting effects of the short-period wavefield and are shown in figure 7. These include distance-time windows containing *P* and *PcP* (figure 7A), the *P* to P_{diff} transition (figure 7B), *PcP* and *ScP* (figure 7C), *PP* from 80° to 120° (figure 7D), *PKiKP* and *PKP* (figure 7E), and the major arc core phases *PKKP* and *SKKP* (figure 7F).

Figure 7(A) shows that the amount of energy in the 1 Hz *PP* arrivals is relatively low compared with direct *P* (and P_{diff}). This is likely due to scattering and attenuation in the uppermost mantle in the vicinity of the *PP* reflection point. This scattering arises due to the small-scale structure of the lithosphere and the crust, reducing *PP* amplitudes. Another interesting observation indicating a similar mechanism is shown in figure 7(B). Amplitudes of P_{diff} quickly decay past the ray-theoretical transition of *P* to P_{diff} at ~98.4° (for a surface focus in PREM: Dziewonski and Anderson 1981). Almost no short-period P_{diff} is detectable for distances larger than 108°. This is in stark contrast to long-period P_{diff} that can be detected out to 150° (*e.g.*, Wysession *et al.* 1995; Astiz *et al.* 1996). While a loss of high frequencies with increasing diffraction path length is expected, the rapid disap-

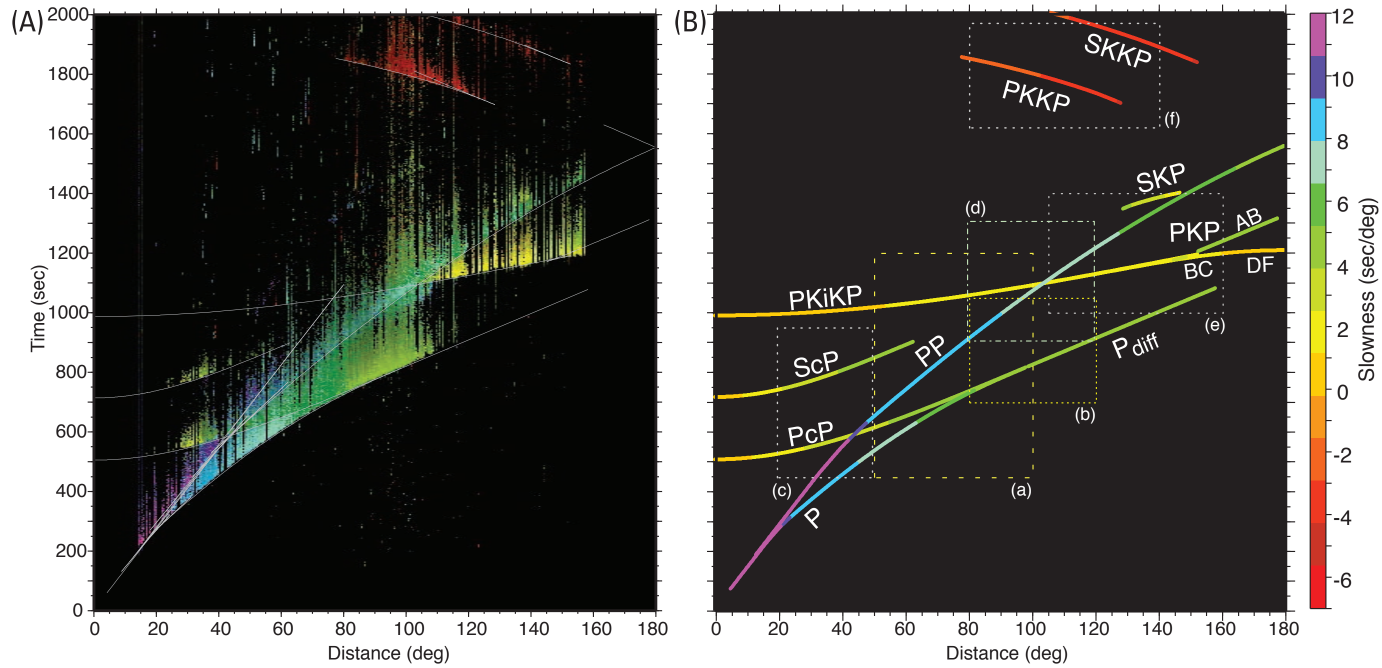

▲ **Figure 6.** (A) Tenth-root vespagram slowness stacks are shown. The slowness information of $ST_{A,u}(t)$ is used for color-coding. Color brightness indicates beam amplitude with higher beam powers more brightly lit. The brightness within each slowness interval is calculated along a hyperbola with a nonlinear factor of 0.6. Thin white lines indicate travel-time curves calculated for PREM (Dziewonski and Anderson 1981). (B) Travel-time curves with slowness of the arrivals color coded as in figure 6(A). Only phases identified in the slowness stacks are shown. Dashed rectangles indicate zoom regions for slowness stacks shown in figure 7.

pearance of the P_{diff} is not predicted by standard reference Earth models. This is likely due to the strong heterogeneity detected at the core-mantle boundary (Garnero 2000), leading to strong scattering of the short-period wavefield (Bataille *et al.* 1990).

Strong precursors to *PP* can be observed in the distance range from 95° to 110° (figure 7D). The slowness-amplitude plots indicate that these precursors show slownesses similar to *PP* and therefore cannot be part of the *P*-wave generated coda. These precursors do not show any coherence in this distance range and are likely not related to underside reflections from the upper mantle discontinuities. Earlier work has shown that these precursors are related to scattering in the upper mantle from asymmetric *PP* reflections due to focusing from the upper mantle velocity structure (King *et al.* 1975; Weber and Wicks, 1996). Recent work shows that energy from asymmetric reflections off the subducted lithosphere may also contribute to this precursory wavefield (Rost *et al.* 2005a).

Core reflected phases (*e.g., ScP* and *PcP*) have been used to probe the small-scale structure of the core-mantle boundary. The global short-period stacks show the small distance window in which these phases normally can be observed. We detect this energy only for distance from 30° to 40°, with the highest amplitudes for *PcP* between 30° and 35°, and 35° to 40° for *ScP*. No coherent precursor to these phases can be identified in the global stacks, indicating that any possible reflector above the core-mantle boundary shows strong topography or can be only detected regionally, which would prohibit a coherent stack of the *PcP* (or *ScP*) precursory arrivals.

▶ **Figure 7.** Zoom into several travel-time distance windows. Left column shows the slowness amplitude stacks as in figure 6(A); the middle column shows stacks including travel-time curves for PREM (Dziewonski and Anderson 1981). Travel-time curves are colored according to slowness using the same color scale used for the slowness amplitude stack. The right column shows the color-coded travel times alone. The fourth column shows globes indicating ray paths for phases shown in the travel-time–distance range in the previous three columns. The distance used for ray tracing is marked by the blue arrow in the third column. (A) Distance range from 50° to 100° and travel times from 450 s to 1,200 s is shown. Phases in this distance–travel-time space include *P*, P_{diff}, *PcP*, *PP* and some slight indication of *S*-wave energy recorded on the vertical instruments. (B) Distance range from 80° to 120° showing the transition from *P* to P_{diff} and the crossover of *P* and *PcP*. (C) Distance from 20° to 50° focusing on the core reflected phases *PcP* and *ScP*. Especially *ScP* can only be detected within a very small distance range in these global stacks. *PcP* shows large amplitudes in a small distance range from 28° to 38° (Rost and Revenaugh 2004). (D) Detection of *PP* in the distance range from 80° to 120°. Precursory energy to *PP* with *PP* slowness that cannot be attributed to P–P_{diff} coda can be detected for distances from ~95° to 110°. (E) Detection of minor arc core phases *PKiKP* and *PKP*. The *PKP* triplication around 150° can be easily detected in the short-period data. (F) Detection of major arc core phases *PKKP* and *SKKP* in the distance range from 95° to 125°. The ab and bc branches of *PKKP* can be identified with $PKKP_{ab}$ being observable several degrees into the core shadow (Rost and Garnero 2006). *SKKP* can be seen only weakly in the stack.

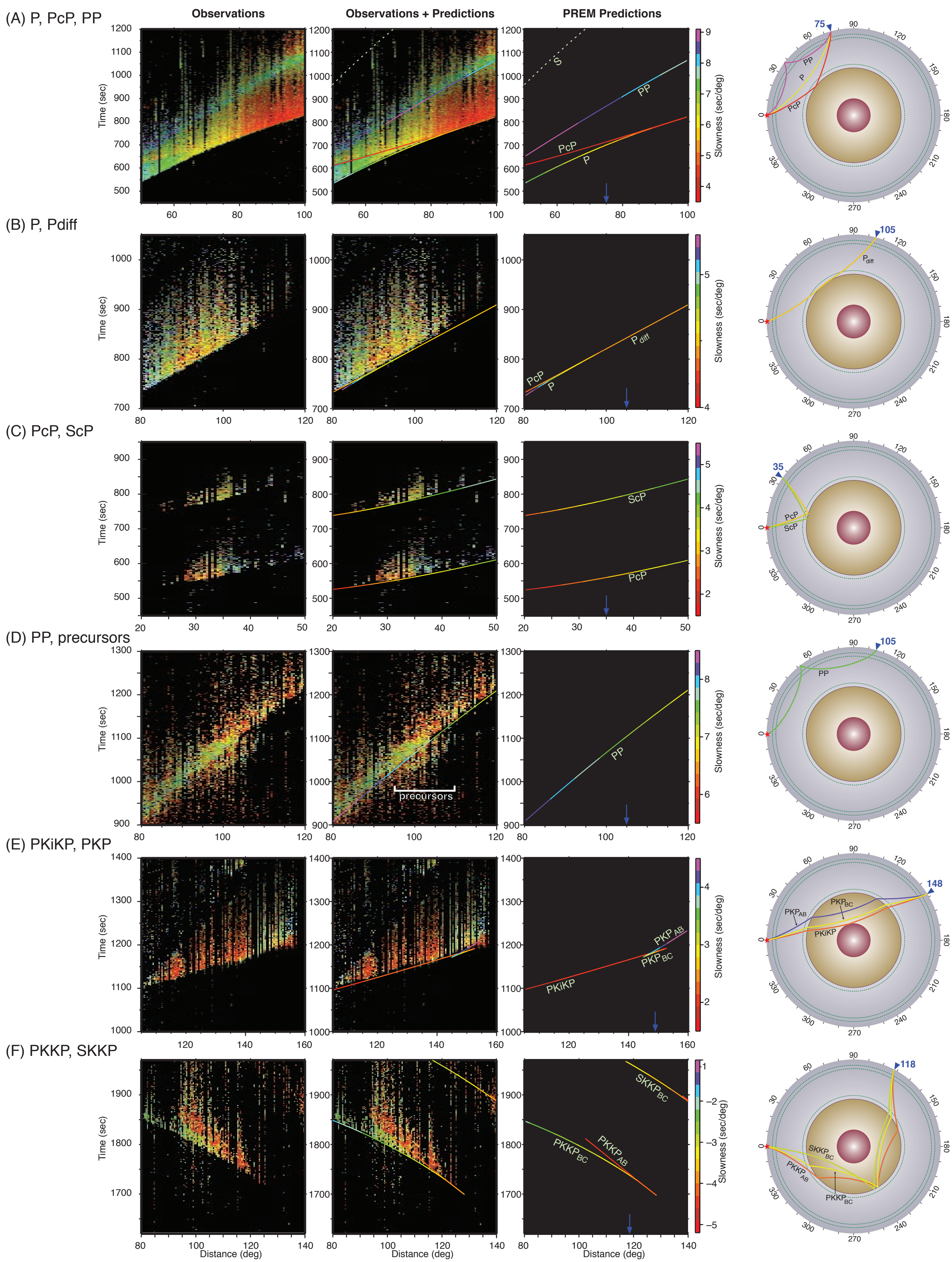
(A) P, PcP, PP
Observations
Observations + Predictions
PREM Predictions
Time (sec)
Slowness (sec/deg)
S
PP
PcP
P
75
(B) P, Pdiff
Pdiff
105
(C) PcP, ScP
ScP
35
(D) PP, precursors
precursors
(E) PKiKP, PKP
PKiKP
PKPAB
PKPBC
148
(F) PKKP, SKKP
SKKPBC
PKKPBC
PKKPAB
118
Distance (deg)

Generating global stacks of processed array data provides a good overview of the high-frequency response of the Earth. Many seismic phases that are observed in long-period data are not observed in our short-period dataset. For example, we do not observe phases such as *PPP*, *PPPP*, or *PKPPcP*. These phases travel long paths and/or contain multiple reflections at the surface or internal boundaries. Therefore, their short-period energy content is probably too weak to see due to the high scattering potential of the Earth's mantle and its boundary layers. Nevertheless, several observations from these global stacks (such as the *PP* precursors and the rapid decay of P_{diff}) justify more in-depth research.

All software required to generate figures as shown in figures 6 and 7 is available from http://array-seismology.asu.edu. Additionally we also supply the stack traces, $ST_{A,u}(t)$, for the YKA data as an example dataset. These tools have exceptional potential as educational tools. Several steps are necessary for the processing from the original array recordings to the stacks shown in figures 6 and 7. We only describe the steps necessary after calculating the original vespagrams $s(t,u)$. Several software tools to calculate vespagrams are freely available (*e.g.*, SeismicHandler by Klaus Stammler available at http://www.szgrf.bgr.de/softarchive.html or the Generic Array Processing code by Keith Koper available at http://www.eas.slu.edu/People/KKoper/Free/index.html).

The MATLAB® script *stacktrace_sh.m* is used to read in the vespagrams in the Q-file format native to SeismicHandler. For reading vespagrams in ASCII format generated by other techniques we provide the script *stacktrace_raw.m*. The input for *stacktrace_raw.m* should consist of data files organized with eight header lines followed by a matrix containing the data. These data files should be organized as follows:

Variable	*Units*
dt	(s)
epicentral distance	(deg)
event origin time	(s)
trace origin time	(s)
event depth	(km)
event longitude	(deg)
event latitude	(deg)
event azimuth	(deg)

$$\begin{bmatrix} u_1 & A_{11} & A_{12} & \cdots & A_{1n} \\ u_2 & A_{21} & A_{22} & \cdots & A_{2n} \\ \vdots & \vdots & \vdots & \ddots & \vdots \\ u_m & A_{m1} & A_{m2} & \cdots & A_{mn} \end{bmatrix}$$

Each row in the matrix contains the amplitudes (A) of each data trace at each slowness (u). Here the index n corresponds to the nth point of the trace with slowness index m.

The scripts *stacktrace_sh.m* and *stacktrace_raw.m* calculate $ST(u,t)$ from the vespagram input. The script *stacktrace_sh.m* requires the functions *rqbn.m* and *rqhd.m* to interpret the SeismicHandler binary and header files. Both scripts *stacktrace_sh.m* and *stacktrace_raw.m* require the files *P_ttimes.xy* (containing the approximate times of first arrivals) and *filelist* (containing the list of vespagrams to process in ASCII format one event per line). The script *Raw_Amplitude_Plot.m* can be used to create basic plots of the stacked traces.

To create slowness-amplitude plots of the stacked $ST(u,t)$ we provide a MATLAB® graphical user interface (GUI) that can be used to create figures as shown in figures 6 and 7. Further information on how to use the GUI can be found in the quickstart guide (http://array-seismology.asu.edu/data/quickstart.html).

CONCLUSION

We have produced an image of the Earth's response to excitation by short-period seismic energy. We have stacked array recordings of 1,224 shallow depth earthquakes resulting in more than 20,000 event-station pairs for the Yellowknife array. Array measurements yield slowness, amplitude, and timing information from the seismic wavefield. We have taken advantage of this information to produce new global stacks highlighting both the amount of energy contained in seismic arrivals, and, through slowness, the direction from which they arrive.

ACKNOWLEDGMENTS

We are grateful for the data from EarthquakesCanada of the Geological Survey of Canada (http://earthquakescanada.nrcan.gc.ca). Data were collected through AutoDRM (Kradolfer 1993). Figures were produced using GMT (Wessel and Smith 1998). We thank Klaus Stammler for his SeismicHandler Software (Stammler 1993). This study was supported in part by National Science Foundation grants EAR-0135119 (E.J.G. and M.S.T.) and EAR-0510926 (S.R.).

REFERENCES

Allen, R. (1982). Automatic phase pickers—their present use and future prospects. *Bulletin of the Seismological Society of America* **72**, S225–S242.

Astiz, L., P. Earle, and P. Shearer (1996). Global stacking of broadband seismograms. *Seismological Research Letters* **67**, 8–18.

Bataille. K., R. S. Wu, and S. M. Flatte (1990). Inhomogeneities near the core-mantle boundary evidenced from scattered waves—a review. *Pure and Applied Geophysics* **132**, 151–173.

Birtill, J. W., and F. E. Whiteway (1965). The application of phased arrays to the analysis of seismic body waves. *Philosophical Transactions of the Royal Society of London, Series A* **258**, 321–493.

Davies, D., E. J. Kelly, and J. R. Filson (1971). Vespa process for the analysis of seismic signals. *Nature—Physical Science* **232**, 8–13.

Dziewonski, A. M., and D. L. Anderson (1981). Preliminary reference Earth model. *Physics of the Earth and Planetary Interiors* **25**, 297–356.

Earle, P. S. (1999). Polarization of the Earth's teleseismic wave field. *Geophysical Journal International* **139**, 1–8.

Garnero, E. (2000). Heterogeneity of the lowermost mantle. *Annual Review of Earth and Planetary Sciences* **28**, 509–537.

Green, P. E., R. A. Frosch, and C. F. Romney (1965). Principles of an experimental large aperture seismic array *(LASA). Proceedings of the IEEE (Institute of Electrical and Electronics Engineers)* **53**, 1,821–1,833.

Haubrich, R. A. (1968). Array design. *Bulletin of the Seismological Society of America* **58**, 977–991.

Kanasewich, E. R., C. D. Hemmings, and T. Alpaslan (1973). *N*th root stack nonlinear multichannel filter. *Geophysics* **38**, 327–338.

King, D. W., R. A. W. Haddon, and E. S. Husebye (1975). Precursors to PP. *Physics of the Earth and Planetary Interiors* **10**, 103–127.

Koper, K. D., and M. L. Pyle (2004). Observations of *PKiKP/PcP* amplitude ratios and implications for Earth structure at the boundaries of the liquid core. *Journal of Geophysical Research* **109**(B03301), doi: 10.1029/2003JB002750.

Koper, K. D., and M. Dombrovskaya (2005). Seismic properties of the inner core boundary from *PKiKP/P* amplitude ratios. *Earth and Planetary Science Letters* **237**, 680–694.

Kradolfer, U. (1993). Automating the exchange of earthquake information. *Eos, Transactions of the American Geophysical Union* **74**, 442, 444–445.

McFadden, P. L., B. J. Drummond, and S. Kravis (1986). The *n*th-root stack—theory, applications, and examples. *Geophysics* **51**, 1,879–1,892.

Rost, S., and E. J. Garnero (2004). Array seismology advances research into Earth's interior. *Eos, Transactions of the American Geophysical Union* **85**, 301, 305–306.

Rost, S., and E. J. Garnero (2006). Detection of an ultra-low velocity zone at the CMB using diffracted $PKKP_{ab}$ waves. *Journal of Geophysical Research*, forthcoming.

Rost, S., and J. Revenaugh (2004). Small-scale changes of core-mantle boundary reflectivity studied using core reflected *PcP*. *Physics of the Earth and Planetary Interiors* **145**, 19–36.

Rost, S., and C. Thomas (2002). Array seismology: Methods and applications. *Reviews of Geophysics* **40** (3), doi: 10.1029/2000RG000100.

Rost, S., E. J. Garnero, A. McNamara, Q. Williams, and D. Zhao (2005a). Detection of subducted lithosphere in the midmantle from asymmetric *PP* reflections. *Eos, Transactions of the American Geophysical Union Supplement,* DI41A-1254.

Rost, S., E. J. Garnero, Q. Williams, and M. Manga (2005b). Seismological constraints on a possible plume root at the core-mantle boundary. *Nature* **435**, 666–669.

Schimmel, M., and H. Paulssen (1997). Noise reduction and detection of weak, coherent signals through phase-weighted stacks. *Geophysics Journal International* **130**, 497–505.

Shearer, P. (1991). Imaging global body wave phases by stacking long-period seismograms. *Journal of Geophysical Research* **96**, 20,353–20,364.

Stammler, K. (1993). SeismicHandler: Programmable multichannel data handler for interactive and automatic processing of seismological analyses. *Computers & Geosciences* ***19***, 135–140.

Taner, M. T., F. Koehler, and R. E. Sheriff (1979). Complex seismic trace analysis. *Geophysics* **44**, 1,041–1,063.

Vidale, J. E., and H. M. Benz (1993). A sharp flat section of the core mantle boundary. *Nature* **359**, 627–629.

Vidale, J. E., and P. S. Earle (2000). Fine-scale heterogeneities in the Earth's inner core. *Nature* **404**, 273–275.

Weber, M., and C. W. Wicks (1996). Reflections from a distant subduction zone. *Geophysical Research Letters* **23**, 1,453–1,456.

Weichert, D. H., and K. Whitham (1969). Calibration of the Yellowknife seismic array with first zone explosions. *Geophysical Journal of the Royal Astronomical Society* **18**, 461–476.

Wessel, P., and W. H. F. Smith (1998). New, improved version of the Generic Mapping Tools released. *Eos, Transactions of the American Geophysical Union* **79**, 579.

Wysession, M. E., R. W. Valenzuela, A. N. Zhu, and L. Bartko (1995). Investigating the base of the mantle using differential travel times. *Physics of the Earth and Planetary Interiors* **92**, 67–84.

School of Earth and Environment
Earth Sciences
The University of Leeds
Leeds, LS6 9JT U.K.
srost@earth.leeds.ac.uk
(S.R.)

Arctic Region Supercomputing Center
University of Alaska Fairbanks
909 Koyukuk Drive, Suite 105
P.O. Box 756020
Fairbanks, Alaska 99775-6020 U.S.A
mthorne@gi.alaska.edu
(M.S.T.)

School of Earth and Space Exploration
Arizona State University
Box 871404
Tempe, Arizona 85287-1404 U.S.A.
garnero@asu.edu
(E.J.G.)